This article has been accepted for publication in a future issue of this journal, but has not been fully edited. Content may change prior to final publication. Citation information: DOI 10.1109/TMRB.2021.3118304, IEEE Transactions on Medical Robotics and Bionics

Online needle-tissue interaction model identification for force feedback enhancement in robot-assisted interventional procedures

Marco Ferro, Claudio Gaz, Michele Anzidei, and Marilena Vendittelli

***Abstract*—Many interventional procedures, e.g., biopsies and tumor ablation, imply the insertion of a needle into soft tissues. The interaction force at the needle tip can convey information important for the accuracy of needle placement and the patient's safety. This information is essential when feedback from an imaging system is missing or only available at a low rate. To isolate the force exchanged at the needle tip during the insertion, it is necessary to remove other components from the needle-tissue interaction force. In particular, the friction along the needle shaft becomes more and more relevant as the needle penetrates deeper into the tissues. In this paper, we propose a method for the identification of the friction component during needle penetration into a multi-layered target. The proposed online identification procedure allows, at the transition from one tissue layer to the next, to subtract the friction contribution from the previous layers and isolate the force relative to the layer where the needle tip is currently located. We call this an *enhanced* force signal because it improves the ratio of the useful information about the force at the needle tip to the total force rendered. This result can be used in teleoperated needle insertion schemes, or other robot-assisted architectures, with the aim of facilitating the user perception of variations in tissue properties. In the proposed implementation, the force at the base of the needle can either be measured or estimated by using a model-based approach. An originally developed simulation framework provides a tool for procedure planning and online monitoring.**

***Index Terms*—needle insertion procedures, needle-tissue interaction estimation, force enhancement, 3D surgical simulator.**

I. Introduction

NEEDLE insertion in soft tissues is today routinely executed in many interventional procedures with diagnostic or therapeutic purposes. The insertion is very often executed blindly or with a feedback from imaging devices at a low refresh rate. Poor visual feedback can, in principle, be compensated by haptic information [1]. In particular, the force exchanged at the needle tip conveys important information about puncturing or cutting of layers encapsulating critical structures or pathological targets. This force, however, is difficult to perceive without a finely trained sense of touch. In fact, as the needle penetrates deeper into tissues, the friction along the needle shaft becomes more and more relevant and can prevent the correct perception of the interaction state at the needle tip. This problem has led to the development of devices, e.g., [2], for manual needle insertion, that mechanically decouple the needle-tissue interaction force component due to friction from the force exchanged at the needle tip.

The appropriate rendering of the force at the needle tip is even more important if it is inserted through a remotely operated robotic manipulator because, in this case, other factors may concur in degrading the transparency of teleoperation. In fact, the introduction of robots and robotic technologies in interventional procedures is today the subject of a lively research and innovation activity because they are useful to protect the medical staff when imaging techniques based on ionizing radiations are used (e.g., computerized tomography or fluoroscopy), to comply with the narrow workspace of the imaging devices bore, and to provide to the operator an enhanced and augmented information. Teleoperation is key to address the above mentioned requirements. Currently available commercial systems [3]–[5] exploit only partially the potentialities of robotics technologies. Even though featuring automatic needle alignment guided by images, all of them lack in the use of real-time imaging and require manual, blind, needle insertion. Recently, a fully automatic system for needle insertion has reached the market [6] which, however, does not allow real-time correction of the needle path and cannot be operated remotely.

The motivation of this work is to provide an *enhanced* force feedback in teleoperated systems. To pursue this objective, it is necessary to properly model the needle-tissue interaction force, along with its relevant and dominant contributions. One of the first modeling efforts is due to the seminal work [7] that distinguishes three main components within the needle-tissue interaction model: a *stiffness* force, defined through a nonlinear spring model and mainly due to tissue puncturing by the needle tip; a *friction* force, collecting static, dynamic and damping friction along the needle shaft; a *cutting* force at the needle tip, modeled with a constant term. Validation and experimental studies have been conducted to accurately describe these force components [8], [9]. An analytical formulation of the biomechanics underlying the needle insertion, has been proposed recently [10]. The provided formulation extends the categorization of the force components in order to explicitly determine tissue puncturing and rupture phenomena, as well as deformation forces acting on the needle shaft. The puncturing force is expressed by a visco-elastic model, while a nonlinear model accounting for pre-sliding, break-away and sliding effects is considered to describe the friction force. Energy-based formulations are exploited to formalize tissue ruptures and to determine the cutting force component.

The models presented in the above cited works offer a

M. Ferro, C. Gaz and M. Vendittelli are with the Dipartimento di Ingegneria Informatica, Automatica e Gestionale, Sapienza Università di Roma, Via Ariosto 25, 00185 Roma, Italy; e-mail: {ferro,gaz,vendittelli}@diag.uniroma1.it.

M. Anzidei is with Centro SaNa,Via Peschiera 04011 Aprilia (LT), Italy; e-mail: michele.anzidei@gmail.com.

Marco Ferro is the corresponding author.

strong and robust reference in the description of the interaction forces, obtained through an extensive analytical effort and a large number of available insertion datasets that are processed *offline*. This setup is obviously unfeasible if the needle insertion state (e.g., interaction force, needle deflection) needs to be predicted in an *online* fashion during the execution of a percutaneous procedure. In this case, simpler models should be preferable, and the effort in determining the appropriate ones may differ in the methodology used for their derivation, in the intended use of models, and in the assumptions taken.

Analytical models are suited to online identification of model parameters for real-time force prediction and rendering. Within this perspective, models describing the interaction force as a combination of an elastic and a damping component are typically employed [1], [11], [12].

In [11], visco-elastic models are used to define control schemes for the interaction between robots and soft bodies considering only contact forces, without puncturing or cutting events. An interaction force model suitable to needle insertion in multi-layered volumes, i.e., taking into account needle penetration into layers, has been proposed in [1]. In this model the elastic component is associated to puncturing phenomena occurring at the needle tip, while a friction term accounts for needle shaft penetration inside tissues.

In [12], the problem of online identification of the interaction force model in percutaneous needle insertions is solved with the objective of producing a reliable prediction of the interaction force. No guarantee about the physical plausibility of the identified model parameters is, however, provided. This is structurally implied by the adopted identification procedure aiming at predicting the total force only, with the ultimate goal of detecting tissue ruptures. The work in [13] extends the procedure to a multi-layer tissue model but shares the limitation of [12] in the physical accuracy of the identified parameters value. The very recent work [14] addresses the problem of estimating the friction along the needle shaft, but does not consider the multi-layer tissue model, relies on US imaging and offline preliminary insertion experiments aiming at identifying an average friction force per unit length.

In this paper, we present an identification procedure providing not only an accurate prediction of the total force due to the interaction of a rigid needle with multi-layered tissues, but also of the main components of this force. Adopting a visco-elastic interaction model, this will enable to render the force exchanged at the needle tip by removing the viscous component, arising along the needle shaft, from the total force. We propose the implementation of this procedure using either measurements from a force/torque (F/T) sensor at the base of the needle, or model-based interaction force estimation methods [15]. With respect to [13], we provide in the present study a refined identification model based and a new identification procedure improving the adherence of the identified components to the real ones. The proposed approach does not need information from imaging nor a preliminary offline estimation of the friction per unit length because it exploits the information from rupture events in an original way, as will be explained in Sect. III-B.

The original contribution of the presented work can be summarized in the following points: i) a new *online* identification procedure providing physically plausible values of the force model parameters; the procedure takes advantage of the information provided by rupture events and does not require additional information from imaging devices and/or prior information about the friction characteristics of the tissue to be punctured; ii) an extensive experimental validation and comparison of dynamic needle-tissue interaction models in synthetic multi-layered environments; iii) experimental validation of the identification procedure using information about the interaction force coming either from a F/T sensor or from a momentum observer of the robot executing the insertion; iv) the development of an integrated environment including a 3D simulator that integrates the different technological components of the setup.

The paper is organized as follows: in Section II two visco-elastic interaction models are analysed, resorting to a systematic offline analysis, with the aim to provide a ground truth reference for the online identification, described in Sec. III. Section IV summarizes a method for the estimation of the total interaction force based on the robot model. When used in combination with the proposed identification procedure, this estimate of the force is shown to represent a valid alternative to force measurement. In Section V, the software architecture of the whole framework is described. Section VI discusses the experimental results obtained in the validation of the proposed force identification and enhancement method. Finally, Section VII concludes the paper and draws directions of future research.

II. Offline identification of needle-tissue interaction dynamics

This section presents the results of preliminary experiments for *offline* parameter identification of two different interaction models. The identified parameters will be used as reference values for the validation of the *online* identification algorithm described in the next Sect. III. Note that, both the offline and the online procedures rely on the following assumptions: i) the needle-tissue interaction force is described by a linear visco-elastic model; ii) the force arising in the i-th layer depends only on the stiffness and the friction characteristics of tissue in layer i and of the preceding layers $j = 1, \dots, i-1$. Interaction with layer $i+1$ arise only during the puncturing phase of this layer as a damping component. This contribution is collected in the friction of the layer i. If the puncturing occurs at the first layer, this will result in the definition of a fictitious layer, as will be explained later; iii) the biomechanical properties of the traversed tissues are homogeneous over the geometry of the target; iv) the interaction force cannot grow unbounded: force growth is either followed by a sudden force drop or the needle is completely inserted into the tissue, and the procedure stops. Layer thickness and tissue rupture events are instead assumed to be known in the offline analysis, while no a priori information about the target geometry is available online.

In the considered operative setup, a surgical rigid unbeveled-tip needle is mounted at the end-effector of a robotic manipulator and inserted through different tissue layers stacked on each other (see Fig. 1a). The interaction force can be expressed through a linear visco-elastic relationship as [12]:

$$f(t) = f_K(t) + f_B(t) = \boldsymbol{\varphi}^T \boldsymbol{\theta} \tag{1}$$

This article has been accepted for publication in a future issue of this journal, but has not been fully edited. Content may change prior to final publication. Citation information: DOI 10.1109/TMRB.2021.3118304, IEEE Transactions on Medical Robotics and Bionics

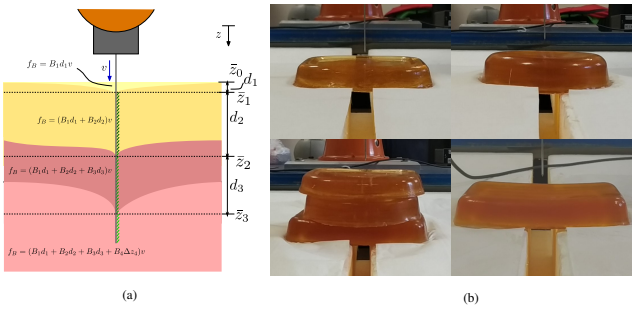

Fig. 1: (a) Schematic representation of a needle insertion through different tissue types, with the expression of the force components acting on the needle in each layer; (b) Four examples of isinglass phantoms used in the proposed analysis. From top-left, in clockwise order: targets with 25%, 50% and 70% isinglass solution and a composed multi-layer gel phantom.

where $f_K(t)$ and $f_B(t)$ are respectively the elastic and friction components of the force. In vector notation it is expressed through the input vector $\boldsymbol{\varphi}$ and the parameter vector $\boldsymbol{\theta}$. Denoting by $z(t)$ the needle tip position along the insertion axis, and by $v(t)$ the corresponding velocity, the generalized Kelvin-Voigt (KV) model specifies Eq. (1) as [12]:

$$\begin{aligned} f(t) &= -K(t)z(t) - B(t)v(t) \\ &= \begin{pmatrix} -z(t) & -v(t) \end{pmatrix} \begin{pmatrix} K(t) & B(t) \end{pmatrix}^T, \end{aligned} \tag{2}$$

where $K(t)$ is a time-varying stiffness coefficient collecting elastic contributions of the interaction and $B(t)$ is the time-varying viscous friction coefficient of the tissue in contact with the needle. In this model, the friction force $f_B(t) = B(t)v(t)$ does not depend on the needle tip position $z(t)$ and the damping components of the force due to the interaction of the needle shaft with the penetrated layers of tissue are neglected.

The KV model formulation (2) can be adapted to allow the consideration of a multi-layer target tissue. To this end, a damping component, which depends on the penetration depth, is introduced in the force [1]:

$$\begin{aligned} f(t) &= -K_i(t)\Delta z_i(t) - B_i(t)\Delta z_i(t)v(t) - \bar{B}_d v(t) \\ &= -\begin{pmatrix} \Delta z_i & \Delta z_i v & v \end{pmatrix} \begin{pmatrix} K_i & B_i & \bar{B}_d \end{pmatrix}^T, \end{aligned} \tag{3}$$

where we have dropped time dependencies in the second line. In the above model, $\Delta z_i(t) = z(t) - \bar{z}_{i-1}$ is the needle tip relative penetration inside the i-th layer L_i which starts at $\bar{z}_{i-1}$, K_i and B_i are the stiffness and friction coefficients, d_i is the layer thickness along the insertion axis and $\bar{B}_d = \sum_{j=1}^{i-1} B_j d_j$ is the constant cumulative friction term due to contact of the needle shaft with the previous layers L_j, with $j = 1, \ldots, i-1$.

Differently from Eq. (2), the friction force in Eq. (3) is a function also of the needle displacement Δz_i , representing the amount of needle shaft in contact with the layer L_i of the tissue. Furthermore, current and cumulative friction terms are kept separated to preserve the model linearity with respect to its parameters. Henceforth, we will denote Eq. (3) as *multi-layer* (ML) model.

The result of the following offline analysis suggests that ML has a better descriptive potential with respect to KV. The experimental setup includes a set of isinglass phantoms that have been realized in such a way to preserve – at best – density homogeneity for each of the different layers. The objective is to acquire a priori information on the B_i parameters to be used later, as a ground truth, in the validation of the online procedure. We prepared gel phantoms with 25%, 50% and 70% isinglass solution and considered stacks with different combinations of these three layers. Stacks have been placed over a pair of separated panels, to allow the needle to completely traverse the phantom (see Fig. 1b). In this way, the force measured when the needle tip exits the phantom, at the opposite point of the entry, is dominated by the friction component due to the adherence of the shaft to the tissue [7], [9], [16].

For each stack, we performed autonomous insertions with constant and time-varying (sinusoidal profile) velocity through a KUKA LWR 4+ robot manipulator, equipped with an ATI Mini45 6D Force/Torque sensor and an unbeveled-tip needle at its end-effector. For each insertion, we observed the entire F/T sensor force signal $\boldsymbol{f}(t)$ over time and manually determined the instants t_i corresponding to transitions from layer L_{i-1} to L_i, such that $z(t_i) = \bar{z}_i$. Hence, we built the input signals:

$$\begin{aligned} \varphi_{K_i}(t, t_i, t_{i+1}) &= \begin{cases} \Delta z_i, & t_i < t \leq t_{i+1} \\ 0, & \text{otherwise} \end{cases}, \\ \varphi_{B_i}(t, t_i, t_{i+1}) &= \begin{cases} \Delta z_i v, & t_i < t \leq t_{i+1} \\ d_i v, & t \geq t_{i+1} \\ 0, & \text{otherwise} \end{cases} \end{aligned} \tag{4}$$

where the second case collects in φ_{B_i} also the contribution of the preceding layers that falls in $\bar{B}_d$ in the ML model (3). Note that, it is straightforward to derive a similar expression of $\boldsymbol{\varphi}_{B_i}$ for the KV model (2), by letting $\boldsymbol{\varphi}_{B_i} = v$ for $t \geq t_{i+1}$.

For $i = 1, \ldots, \ell$, being ℓ the number of layers of the target multi-layer tissue, the input signals of Eq. (4) are collected to build the following regression matrix:

$$\boldsymbol{\Phi} = \begin{bmatrix} \boldsymbol{\varphi}_{K_1} & \boldsymbol{\varphi}_{B_1} & \cdots & \boldsymbol{\varphi}_{K_\ell} & \boldsymbol{\varphi}_{B_\ell} \end{bmatrix} \tag{5}$$

and the vector $\boldsymbol{\theta} = (K_1, B_1, \ldots, K_\ell, B_\ell)^T$ is found in a least-square fashion as

$$\hat{\boldsymbol{\theta}} = \boldsymbol{\Phi}^{\#} \boldsymbol{f}. \tag{6}$$

where $^{\#}$ denotes the matrix pseudoinversion operator.

Figure 2 reports the identification and force prediction results for four experiments. In the upper panels, we compared the measured force (green line) with the force predicted by KV and ML models (blue and red lines, respectively). Bottom panels show the reconstruction errors for the two models, with the corresponding Root Mean Square Error (RMSE). In the upper panel of Fig. 2a, the needle enters with constant insertion velocity and completely traverses a 70% isinglass phantom, before the needle tip exits the layer and is completely extracted (with the same velocity, opposite in sign); in Fig. 2b, the same needle motion is repeated with a stack of three layers of 25%, 50% and 70% isinglass phantoms. Analogously, Fig. 2c and Fig. 2d report the result of two experiments for the same pair of phantoms, with sinusoidal motion of the needle. The force signals (a)-(b), related to constant insertion velocity, present similar features: a linear increase – with different slope for each layer – of the measured force (green line) is present as long as the needle traverses the layers, being the tip inside the

This article has been accepted for publication in a future issue of this journal, but has not been fully edited. Content may change prior to final publication. Citation information: DOI 10.1109/TMRB.2021.3118304, IEEE Transactions on Medical Robotics and Bionics

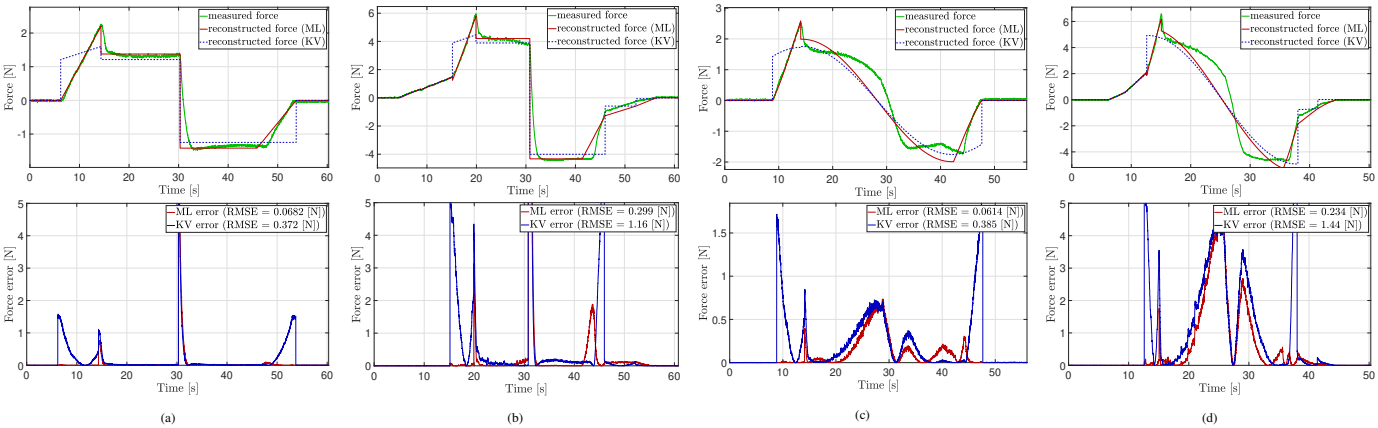

Fig. 2: Comparison of the reconstructed force (top row) and error (bottom row) signals obtained through offline identification, on gel stack phantoms with different isinglass solution layers. Autonomous insertion velocity is constant ((a)-(b)) and sinusoidal ((c)-(d)). Displayed signals are F/T sensor measurement (green), force reconstruction with KV (dashed blue line) and ML model (continuous red line).

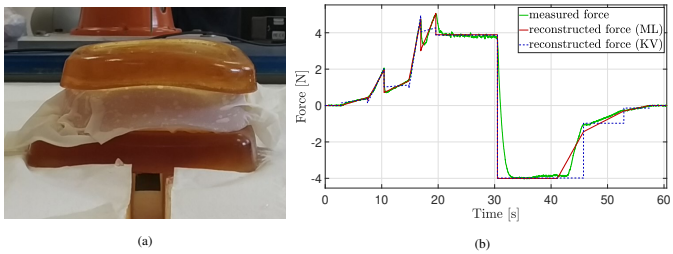

Fig. 3: (a) The three-layered phantom with the latex glove enveloping the intermediate layer. (b) Reconstructed forces with KV (dashed blue line) and ML (continuous red line) models.

phantoms; as soon as the tip exits the layers (approximately at $15s$ in (a) and $20s$ in (b)), a drop in the force is observed and a constant value is retrieved, until the needle stops its motion. When the motion is reversed, the same constant force, but opposite in sign, is detected by the F/T sensor until the needle is completely extracted and the measured force becomes null. The observed plateaux in the force value are due exclusively to friction acting on a portion of the needle shaft of constant length (equal to the sum of the layer thicknesses), being the tip in the free space in the corresponding time interval.

Force signals in (c)-(d), instead, highlight a slightly different behavior due to the sinusoidal motion of the needle. In particular, as highlighted in the bottom plots of Fig. 2, we observe a higher reconstruction error when the needle exits the layers for both models, showing the presence of not modeled force contributions. This is likely due to rigid-soft complex interactions, such as presliding and memory effects, that violate the linearity between the measured force and the input velocity [7], [10]. In the experimental section it will be shown that this does not limit our purpose to identify and compensate for a plausible value of the friction component in the interaction force.

The analysis is concluded with a further experiment in which we used a latex glove to envelop the intermediate phantom of the stack (see Fig. 3a), so as to simulate tissue puncturing and rupture phenomena possibly occurring in transitions between different tissue layers. In this experiment, we modeled the presence of the glove as an additional elastic contribution, formally analogous to φ_K in (4) on the second and third phantom of the stack, i.e., $\boldsymbol{\varphi}_{K_g} = \varphi_{K_i}(t, t_i, t_{r_i})$, where $t_{r_i} \neq t_{i+1}$ is the time instant of the rupture event for the layer L_i. The reconstructed force with both KV and ML models, for constant needle velocity, is shown in Fig. 3b. Also in this case, the visual inspection of the figure clearly shows that the ML model is able to track the signal variations, and capture the relevant signal feature, closer than the KV.

The described offline estimation process has been conducted over 14 datasets corresponding to insertions on different phantoms built as combination of the considered gelatin layers. All the experiments prove that the ML model is more reliable than KV model in capturing the elastic and friction phenomena occurring during the insertions and reconstructing the measured force, as can be also appreciated by the RMSE values reported in the legends of the bottom panels of Fig. 2.

The values of the B_i parameters identified in this phase are reported in Table 10 and used in the discussion of the online procedure results.

III. Online Identification of Needle-Tissue Interaction Dynamics

In the offline analysis of the previous section we have assumed the thickness d_i, and instants t_i and t_{r_i} to be known. This assumption is here removed and the above variables are estimated during the online procedure. In particular, the thickness d_i of the i-th layer is identified for the first layer as the distance traveled by the needle between the first contact and the first rupture. For the subsequent layers, it is set as the distance between two consecutive detected ruptures.

For the online identification of the model parameters, we adopt the methodology based on the Recursive Least-Square (RLS) algorithm, as in [13]. In that work, the interaction force was correctly reconstructed according to the KV model (2), although no assessment was made about the physical consistency of the estimated friction component. Indeed, we have shown in Sect. II that the ML model (3) actually outperforms KV in the offline interaction force reconstruction, thus being a more suitable model choice. The online identification of the ML model with the RLS may, however, incur in observability issues for slowly-varying needle motions which produce poorly

This article has been accepted for publication in a future issue of this journal, but has not been fully edited. Content may change prior to final publication. Citation information: DOI 10.1109/TMRB.2021.3118304, IEEE Transactions on Medical Robotics and Bionics

excited RLS input signals. This can be also highlighted by observing that the portions of the input signals $\boldsymbol{\varphi}_{B_i}$ and $\boldsymbol{\varphi}_{K_i}$ in the regression matrix (5), corresponding to the traversal of an arbitrary layer L_i, are very close to be linearly dependent when the insertion velocity v is almost constant. As a consequence, the online estimated parameters, while accurately reconstructing the measured interaction force, are non-unique and may be even physically unfeasible. Therefore, some expedients in the online identification methodology must be considered, so as to successfully tackle the RLS observability issue due to input excitation and allow to retrieve estimated parameters of the ML model consistently with the offline analysis conducted in Sect. II.

In the following, we will briefly summarize the methodology presented in [13]. Then, we will describe how we modified the approach in order to robustly retrieve physically plausible estimation of the ML model parameters.

A. Online identification methodology

The RLS algorithm reconstructs, for each discrete time instant k, an estimation $\hat{\boldsymbol{\theta}}$ of the tissue layer parameters as:

$$\hat{\boldsymbol{\theta}}_k = \hat{\boldsymbol{\theta}}_{k-1} + \frac{\boldsymbol{\Psi}_{k-1}\boldsymbol{\varphi}_k e_k}{\lambda_k + \boldsymbol{\varphi}_k^T \boldsymbol{\Psi}_{k-1}\boldsymbol{\varphi}_k}, \tag{7}$$

$$\boldsymbol{\Psi}_k = \boldsymbol{\Psi}_{k-1} - \frac{\boldsymbol{\Psi}_{k-1}\boldsymbol{\varphi}_k\boldsymbol{\varphi}_k^T\boldsymbol{\Psi}_{k-1}}{\lambda_k + \boldsymbol{\varphi}_k^T \boldsymbol{\Psi}_{k-1}\boldsymbol{\varphi}_k}, \tag{8}$$

where $\boldsymbol{\Psi}_k$ is the covariance matrix and $\lambda_k \in (0, 1]$ the *forgetting factor*, typically set to 1. Hence, it is possible to evaluate, for each k, the error $e_k = f_k - \hat{f}_k$ between the force f_k, measured by a force sensor on the robot wrist where the needle is mounted, and the predicted force $\hat{f}_k = \boldsymbol{\varphi}_k^T \hat{\boldsymbol{\theta}}_{k-1}$. To foster the algorithm responsiveness to the variations of the mechanical properties of a target multi-layer tissue and allow the parameters estimation to change accordingly, a Covariance Resetting (CR) mechanism is employed.

The transition between two subsequent tissues is automatically detected through the CUSUM algorithm [17], that adopts a specific decision function g depending on the pair of variances σ_0 and σ_1, related to *standard* and *abrupt change* cases, respectively:

$$g_k = \max(g_{k-1} + e_k^2 - \nu, 0) > \gamma \ , \ g_0 = 0, \tag{9}$$

being $\gamma = (\sigma_1^2 - \sigma_0^2)/2$ and $\nu = (\sigma_1^2 + \sigma_0^2)/2$.

Note that, in [13], the effects of the CR condition on the online estimation results are not analysed. Yet, manipulating properly the covariance matrix related to the estimating parameters reveals to play a key role in addressing the input signal excitation problem. It allows, in particular, to retrieve, among the set of possible solutions, estimates of the parameters that are consistent with the values obtained offline. This is discussed in the next Section.

B. Identification procedure refinement

This section illustrates a revision of the online procedure used in [13] consisting in re-weighting, at the end of each traversed layer of the target tissue, the covariance matrix, with consequent re-estimation of the corresponding parameters, based on direct measurements of the *force drops* occurring after tissue ruptures.

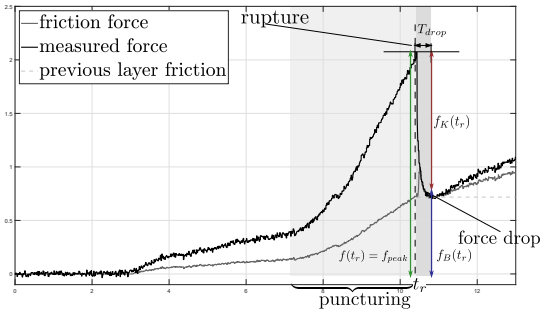

Fig. 4: Relevant intervals and events for the evaluation of the force components distribution in the novel online identification methodology.

In fact, rupture events, and the corresponding force drops in the measured signal, provide reliable information about how elastic and friction contributions are distributed in the measured force. This information is used to re-weight, *a posteriori*, the initial value of the covariance matrix $\boldsymbol{\Psi}_0$. The newly acquired information is then back-propagated by re-running the RLS-CR algorithm on the input data of the latest traversed layer. This drives the algorithm to converge to the parameters that best describe the distribution of the elastic and friction contributions, in accordance with the information provided by the rupture event, while still minimizing the force error.

Specifically, after each detected rupture, the revised procedure considers a waiting interval $T_{drop,i}$ to measure the force drop $f_{drop,i}$ occurring after the rupture. With reference to Fig. 4, we compute $f_{drop,i}$ as

$$f_{drop,i} = f(t_{r_i}) - f(t_{r_i} + T_{drop,i}) \simeq f_K(t_{r_i}). \tag{10}$$

Once $f_{drop,i}$ is properly measured, the elastic and friction force ratio, $r_{K,i}$ and $r_{B,i}$, is determined:

$$r_{K,i} = \begin{cases} \dfrac{f_{drop,i}}{f(t_{r,i})} & , i = 1 \\ \dfrac{f_{drop,i}}{f(t_{r,i}) - \sum_{j=1}^{i-1} \hat{B}_j \hat{d}_j v(t_{r,i})} & , i \geq 2 \end{cases} \tag{11}$$

$$r_{B,i} = 1 - r_{K,i}.$$

In the above equation, $\hat{d}_j$ is the estimate of the j-th layer thickness which is obtained using the detection of the consecutive rupture instants $t_{r_{j-1}}$ and t_{r_j}, achieved through the CUSUM algorithm, as described in Sect. III-A.

At this stage, this latter information allows to assign different weights to the elastic and friction components.

In order to determine the appropriate scale factor of the covariance matrix, we do the following considerations. For a given initialized covariance matrix $\boldsymbol{\Psi}_0 = \text{diag}(\sigma^2_{K_i,0}, \sigma^2_{B_i,0})$, we can formalize the weighting as $\boldsymbol{\Psi}'_0 = \boldsymbol{W}\boldsymbol{\Psi}_0 = \boldsymbol{\Lambda}^T\boldsymbol{\Psi}_\mathbf{0}\boldsymbol{\Lambda}$, with $\boldsymbol{\Lambda} = \text{diag}(w_K, w_B)$. From (7)-(8), it can be shown that applying $\boldsymbol{W}$ to the covariance is equivalent to run a weighted update step of the RLS algorithm with input vector $\boldsymbol{\varphi}' = \boldsymbol{\Lambda}\boldsymbol{\varphi}$. Therefore, we can tackle the problem of poor exciting input signals by first balancing the magnitude of the position and velocity signals, $z(t)$ and $v(t)$, through the weight

This article has been accepted for publication in a future issue of this journal, but has not been fully edited. Content may change prior to final publication. Citation information: DOI 10.1109/TMRB.2021.3118304, IEEE Transactions on Medical Robotics and Bionics

$\boldsymbol{W}_1 = \text{diag}(1, d_i^2/\bar{v}_i^2)$, where $\bar{v}_i$ is the average velocity of the needle while traversing the i-th layer. Then, we consider a further weighting matrix to evaluate the friction per unit length, i.e., $\boldsymbol{W}_2 = \text{diag}(1, 1/d_i^2)$. Finally, we apply a third weight to reflect the evaluated ratios r_{B_i} and r_{K_i} on the variances of the parameters, i.e., $\boldsymbol{W}_3 = \text{diag}(1, r_{B_i}/r_{K_i})$. As a result, the RLS algorithm can be *re-run* with the data collected along the last traversed layer, by considering the re-initialized weighted covariance matrix $\boldsymbol{\Psi}_0' = \boldsymbol{W}_1\boldsymbol{W}_2\boldsymbol{W}_3\boldsymbol{\Psi}_0$, resulting in the following rescaling of the friction variance:

$$\sigma_{B_i',0}^2 = \frac{1}{\bar{v}_i^2}\frac{r_{B_i}}{r_{K_i}} \cdot \sigma_{B_i,0}^2. \tag{12}$$

Further details about the derivation of the reported weights can be found in the accompanying Supplementary material.

Re-weighting the covariance matrix according to (12), and re-estimating the model parameters of the last traversed layer with the modified covariance matrix, force the RLS to converge towards more reliable estimation of stiffness and friction coefficients even in case of non-exciting motion. In particular, for insertion in single-layer isinglass phantoms, we show in Sect. VI that the online estimated parameters are close to the physically plausible values retrieved in the offline analysis, proving the effectiveness of the refinement procedure. It is worth noticing that the back-propagation procedure does not produce unnatural artifacts in the force rendering. The subtraction of a physically feasible friction component at each layer transition will let the user perceive only the interaction force due to the penetration of the tip in the current layer.

Along with the presented covariance re-weighting mechanism, we also mention that, with respect to [13], we revised the CR condition so as to be triggered on a time basis according to a constant reset frequency f_{CR}. In fact, since the CR condition mechanism makes the RLS reactive to the changes in the estimating parameters of the different tissue layers, it can be exploited to artificially increase the excitability of the RLS input signals. This results in an improved force tracking accuracy and in more stable and robust estimated parameters.

It should be noted, however, that this also alters the statistical characteristics of the reconstruction error e_k, making hard for the CUSUM algorithm to distinguish properly between *abrupt change* and *standard* cases for tissue rupture detection. To avoid possibly missing detection, a two-step decision process is implemented in a finite-state machine fashion. The revised procedure considers a force derivative-based condition as second criterion, evaluating the derivative of the measured force and triggers a detection event when the signal exceeds a given threshold β. Additional details and a representation of the finite-state machine associated to the detection algorithm are provided in the Supplementary material.

As last remark, having in mind the assumptions listed at the beginning of Sec. II, we point out that, for the proper online detection of the first tissue layer, the instant t_0 of the first contact with the outer layer, and the corresponding needle tip position $z(t_0) = \bar{z}_0$, are known. If the first layer has a membrane to be punctured, the arising damping component is collected in a friction contribution that will be assigned to a fictitious layer with thickness $d_1 = z(t_{r_1}) - \bar{z}_0$. While this does not reflect the real geometry of the target tissue, it allows to correctly capture the involved interaction component along the insertion and provide more reliable results. The behavior is observed and described in the cumulative friction effect analyzed in Sect. VI-B.

In the presented workflow, we assumed to operate in ideal conditions where a F/T sensor provided a direct measurement of the needle-tissue interaction force during the insertion. This may be not always desirable, particularly if a light and minimalist robotic system is appropriate, e.g., in an interventional scenario. In the next Section, we show how to retrieve an indirect measurement of the interaction force relying on the knowledge of the robot model and based on the robot on-board sensors only, thus realizing a virtual F/T sensor that prevents the use of dedicated devices for force measuring. The proposed method will also account for possible uncertainties in the robot model and consider a refinement process to improve the accuracy of the resulting measurement.

IV. Model-based interaction force estimation

Consider a n-DoFs robot manipulator, employed in the surgical workspace to perform a needle insertion operation; the needle is mounted at the robot end-effector and inserted into tissues to reach a given anatomical target. To retrieve an indirect measurement of the interaction force without relying on external dedicated sensors, we consider and estimation approach based on the computation of the momentum-based observer, also called residual vector [15].

The computation of the residual vector, henceforth $\boldsymbol{r}$, requires a reliable knowledge of the dynamic model of the robot and provides an estimation of the external torques $\boldsymbol{\tau}_c$ acting on the robot joints. It can be proved that, for $t \to \infty$, one gets $\boldsymbol{r} \approx \boldsymbol{\tau}_c$ and, specifically, the residual vector $\boldsymbol{r}$ is a low-pass-filtered version of $\boldsymbol{\tau}_c$.

Assuming that no contact occurs along the kinematic chain of the robot (and integrating the additional dynamic parameters of the needle and its adapter in the dynamic model according to [18]), a corresponding estimation of the 6-D external wrench $\boldsymbol{F}_{ext}$ can be computed from $\boldsymbol{\tau}_c$ as

$$\boldsymbol{F}_{ext} = \boldsymbol{J}_{ee}^{T\#}(\boldsymbol{q})\boldsymbol{\tau}_c \tag{13}$$

being $\boldsymbol{J}_{ee}$ the $6 \times n$ Jacobian matrix at the robot end-effector.

A correct reconstruction of the external contact forces is ensured if we have a perfect knowledge of the dynamic model, obtaining $\boldsymbol{r} = \boldsymbol{\tau}_c = \boldsymbol{0}$ in absence of external forces. In practice, a perfect model is difficult to provide, because of possible unmodeled phenomena or unavailable dynamic parameters. In this case, identification algorithms should be employed [19]–[21], but model inaccuracies may still affect the overall estimation, thus providing a residual $\boldsymbol{r} \neq \boldsymbol{0}$ in absence of external forces. While these inaccuracies should be addressed through finer identification procedures, since the considered needle insertion task involves a limited workspace, we only consider a local refinement (i.e., in the neighborhood of the initial configuration) of the available model-based residual vector, by subtracting an initial offset $\boldsymbol{r}_0$ measured at the initial insertion time instant t_0, so as to obtain $\boldsymbol{r}(t_0) = \boldsymbol{0}$.

The four panels in Fig. 5 report the comparison between the interaction force measured by a real F/T sensor (blue lines),

This article has been accepted for publication in a future issue of this journal, but has not been fully edited. Content may change prior to final publication. Citation information: DOI 10.1109/TMRB.2021.3118304, IEEE Transactions on Medical Robotics and Bionics

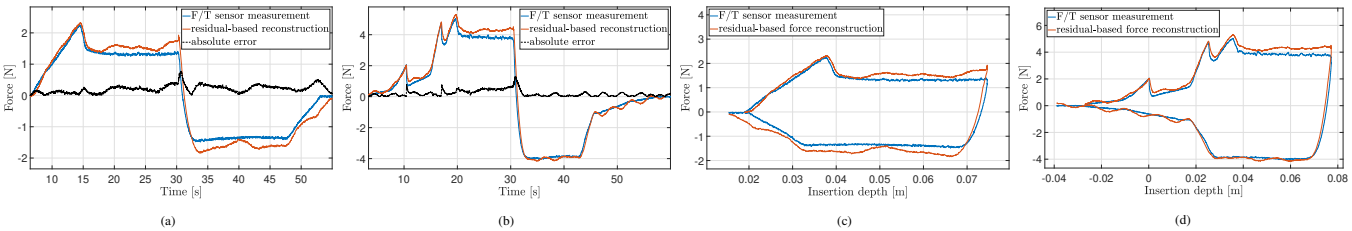

Fig. 5: Results of the residual-based force estimation. In all panels, the blue (red) lines represent the F/T data retrieved (estimated) along the needle axis, during experiments in which the needle traverses completely, with constant velocity, a single gelatin layer (panels (a) and (c)), and a stack of three gelatin layers with a latex tissue enveloping the middle layer (panels (b) and (d)). The needle is retracted after traversing the layers in both experiments. The force estimation error is evaluated as $RMSE = 0.2444$ [N] and $RMSE = 0.285$ [N] for the single-layer and the three-layered-stack phantoms, respectively.

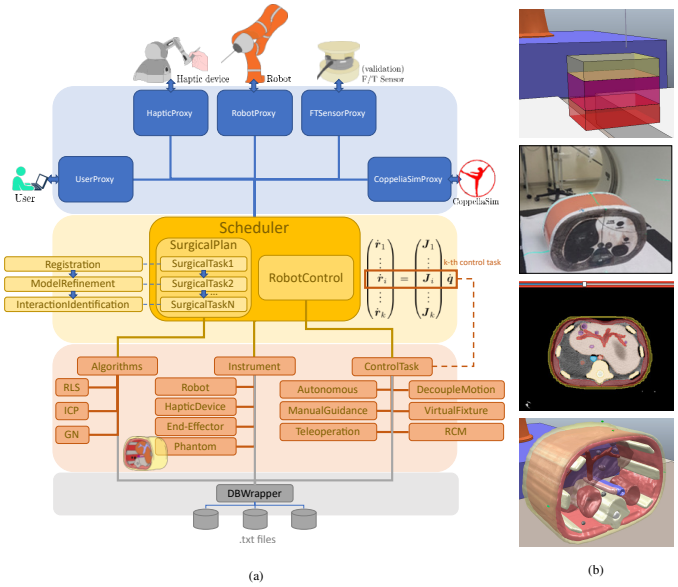

Fig. 6: (a) Software architecture of the framework for robot-assisted needle insertion procedures. (b) 3D modeling of the insertion targets. From top to bottom: the simple multi-layer stack of isinglass gel phantoms; the abdominal phantom under CT scan; intermediate semi-autonomous segmentation and labelling process of the diagnostic scans in 3DSlicer software; the reconstructed 3D model in the virtual scene.

and the reconstruction given by Eq. (13) (red lines): Fig. 5a and Fig. 5b show the two force signals over time, related to insertions with constant velocity in the 70% single-layer phantom and in the three-layered-stack phantom with glove, respectively. The estimation error is highlighted with a black line. Fig. 5c and Fig. 5d show, for the same dataset, the force signals as function of the needle tip position along z.

V. The Interactive Framework

To provide clinicians an assisting tool combining interaction and visual information for surgical procedures, we developed a modular framework with the following features: i) the integration with a set of external systems and devices, including an interactive simulator; ii) a versatile set of robot control and estimation methodologies; iii) a 3D rendering of the target volume of interest. The simulator is based on the dynamic robotic simulation environment CoppeliaSim [22] and models the robot platform with other components of the surgical scenario in a virtual environment. The result is a virtual reconstruction of the needle insertion procedure with enhanced visualization properties, used to assess the progress of the insertion throughout the layers, by providing a visual reference of the detected tissue transitions.

In the remainder of this section, we detail the mentioned features of the framework.

A. Framework architecture

The architecture of the proposed framework is depicted in Fig. 6a and is designed as a multi-layer pattern.

At the top layer (highlighted in blue in in Fig. 6a), a set of proxy objects provide an interface for each external system that requires to be connected with the framework (i.e., robot platform, F/T sensor, CoppeliaSim simulator). To improve the manoeuvrability of the insertion and integrate teleoperation control, we also interfaced a haptic device enabling users to send commands to the robot remotely.

At the middle layer (yellow box in Fig. 6a), we consider objects implementing high-level routines that need to gather and coordinate data from different proxies and objects of higher and lower layers (e.g., robot motion generation, surgical planning and estimation tasks), along with a system manager collecting and scheduling the activities based on user requests or changing environment conditions.

At the lower layer (red in Fig. 6a), a set of abstract objects refer to atomic components of the setup (e.g., robot, target phantom, F/T sensor) or mathematical tools (e.g., algorithms, kinematic constraints), used by the higher-level routines in order to store, load and process local data of each component (e.g., update of the robot kinematics and dynamics, execution of the RLS algorithm), as well as perform write-read operations on the file-system for data logging and storage (gray layer in Fig. 6a).

The resulting system allows to easily implement the necessary aspects for the realization of the needle insertion procedure supported by the robot platform, as well as the fulfillment of the identification task.

B. Robot control

The designed framework provides different robot control modalities and kinematic constraints, guiding the needle motion. The considered control modalities are: i) *manual guidance*, for a rough positioning of the robot through external forces exerted by the user on the manipulator structure; ii) *teleoperation*, for fine regulation, possibly including motion scaling, through the use of a master haptic device; iii) *autonomous*, to automatically perform predefined trajectories. The manual guidance, that enables robot motion by simply

This article has been accepted for publication in a future issue of this journal, but has not been fully edited. Content may change prior to final publication. Citation information: DOI 10.1109/TMRB.2021.3118304, IEEE Transactions on Medical Robotics and Bionics

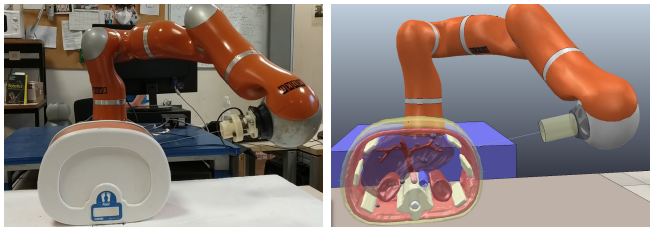

Fig. 7: The integration of the CoppeliaSim simulator in the presented framework: the experimental scenario (left) required for needle insertion procedures is faithfully replicated in real-time in the virtual environment (right).

pushing/pulling it along its kinematic chain, is used to set a first rough placement of the needle tip and is implemented through the residual vector described in Sect. IV. The considered kinematic constraints are: i) *decoupled motion*, to separately set linear and angular velocities and command a more intuitive motion; ii) *virtual fixture*, to constrain the robot to move along the needle shaft direction and prevent undesired lateral motions; iii) *Remote Center of Motion* (*RCM*), to allow needle insertion motion through the entry point in the patient's body, and rotation about the point [23]. Both control modalities and kinematic constraints are modeled as kinematic control tasks. Exploiting the manipulator redundancy, these can be solved simultaneously resorting to a task-priority formulation: we consider a stack of the k assigned tasks expressed in the form $\dot{\boldsymbol{t}}_i = \boldsymbol{J}_i \dot{\boldsymbol{q}}$, with $i = 1, \ldots, k$, and generate the joint velocity vector $\dot{\boldsymbol{q}}$ as a recursive solution, with priorities enforced through task null-space projectors. For the i-th task of the stack, an exponential decay for the task error $\boldsymbol{e}_i = \boldsymbol{t}_{d,i} - \boldsymbol{t}$ is obtained by imposing a linear closed-loop dynamics.

C. 3D target volume modeling

The modeling properties of the CoppeliaSim environment allow to create geometrically simple shapes, through which we may model, e.g., the stacks of isinglass gel phantoms (see top image of Fig. 6b). However, a more rigorous approach is required for volumes with more complex geometry.

For this purpose, we built the 3D model of a medical abdominal phantom from images acquired through 3D CT scan imaging. The modeling process is shown in Fig. 6b: after performing the CT scan on the phantom (second image of Fig. 6b), the acquired images are processed in the 3DSlicer open-source software [24] through semi-autonomous segmentation and labelling tools (third image of Fig. 6b), in order to highlight inner structures, organs and tissues inside the phantom over the three scan axes. The final result is a 3D model of the segmented volumes that is imported in the CoppeliaSim simulated scene (bottom image of Fig. 6b).

To replicate faithfully the real environment where the insertion is performed, an image registration routine is implemented, in order to place the 3D model of the phantom with respect to the robot manipulator, consistently with the real world. The registration procedure is accomplished by collecting a set of landmarks in the 3D model and robot reference frames, estimating the corresponding transformation in a least-square fashion through the ICP algorithm [25]. A complete 3D simulated scene is shown in Fig. 7 and in the accompanying video of this manuscript.

VI. Results

The novel needle-tissue interaction identification algorithm and the integration with the residual-based force measurements have been validated through experiments performed over several targets, with different interaction properties and increasing geometrical complexity: i) isinglass single- and multi-layer phantoms with different solution and latex glove, to increase the elastic behavior during the interaction; ii) a slice of bovine liver; iii) a professional abdomen phantom with inner anatomical structures and organs.

Insertion experiments have been conducted in the same operative conditions described in Sect. II, i.e., considering an empty space below the target to allow full traversal of the considered layers. For the presented experimental results, based on a statistical analysis performed over a number of insertion force signals for each class, we set $\sigma_0 = 0.01$ and $\sigma_1 > 0.08$, while the force derivative threshold is set to $\beta = 0.075$. The CR condition of the RLS algorithm is triggered, with a constant reset frequency $f_{CR} = 40$ Hz. In the following, these classes of experiments are discussed in detail.

A. Experiments on isinglass phantoms

Figure 8 reports the online estimation results for an insertion in a 70% solution target phantom with constant velocity $v = 2.3$ mm/s. The force profile (Fig. 8a) is analogous to the behavior described in Sect. II: a linearly incremental force is sensed by the F/T sensor (green line) during the layer traversal, until an abrupt decrease occurs at the layer exit, bringing the force measurement to a constant value when the needle tip is in the empty space below the phantom. The reconstructed force $\hat{f}$ computed by the RLS (yellow dashed line) fits accurately the measured force, with a spike at the detected rupture instant of the single layer L_1 ($t_{r_1} \simeq 15$ s, shown with vertical black solid line). This spike is due to the discontinuity of $\boldsymbol{\varphi}$ caused by the re-initialization of the initial position $\bar{z}_2 = z(t_{r_1})$, for the expected next layer L_2 (corresponding to the empty space).

To properly measure the force drop at the rupture as described in Sect. III-B, the tissue relaxation time can be modeled as inversely proportional to the insertion velocity [26]. Therefore, we set $T_{drop} = k_v v^{-1}(t_{r_1})$, where $k_v = 1$ is heuristically chosen for all experiments. After $T_{drop,1}$ seconds from the detected rupture (highlighted in vertical dashed black line), the force drop for the current layer is measured and the RLS algorithm is *re-run*, in accordance with Sec. III-B, to generate a robust estimation of elastic and friction coefficients.

Since, at the full traversal of the phantom, the dominating contribution of the measured force is due to the friction between the layer and a constant portion of the needle shaft, an accurate identification will result in an almost zero compensated force after the rupture. From Fig. 8a, we observe that the ML model (red dashed) is more accurate than KV model (yellow dashed), since the corresponding compensated force is closer to 0. In Fig. 8b, the estimated elastic (top panel) and friction (middle panel) coefficients are reported; the

This article has been accepted for publication in a future issue of this journal, but has not been fully edited. Content may change prior to final publication. Citation information: DOI 10.1109/TMRB.2021.3118304, IEEE Transactions on Medical Robotics and Bionics

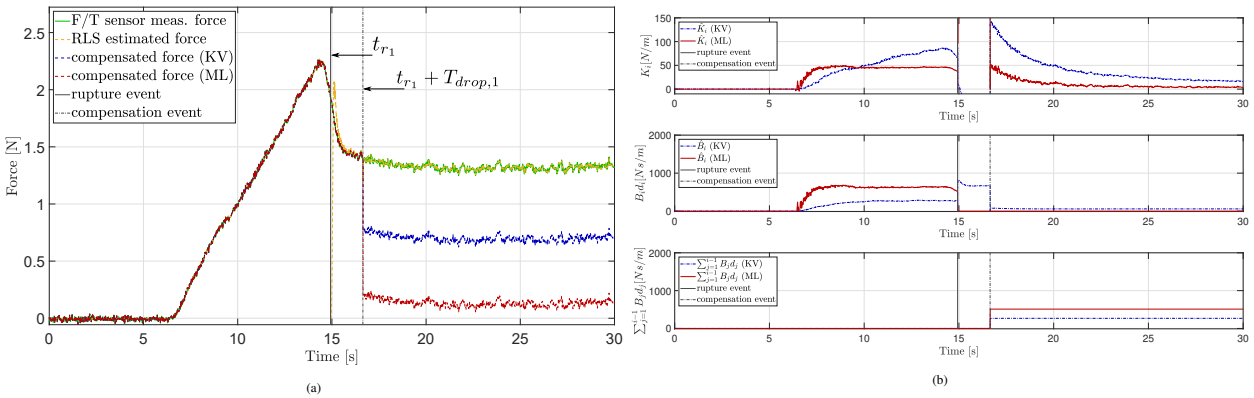

(a) (b)

Fig. 8: Experimental results of the friction compensation algorithm on the 70% solution gel phantom, with unknown layer depth. The needle insertion occurs with a constant velocity. (a) Measured (green), predicted (yellow) and compensated forces using the KV (blue line) and the ML (red line) models. With vertical black lines are highlighted the rupture detection time t_r (continuous line) and the compensation time $t_r + T_{drop}$ (dashed line). (b) Estimation of the elastic (upper panel), local friction (middle panel) and cumulative friction (bottom panel) parameters for the presented experiment.

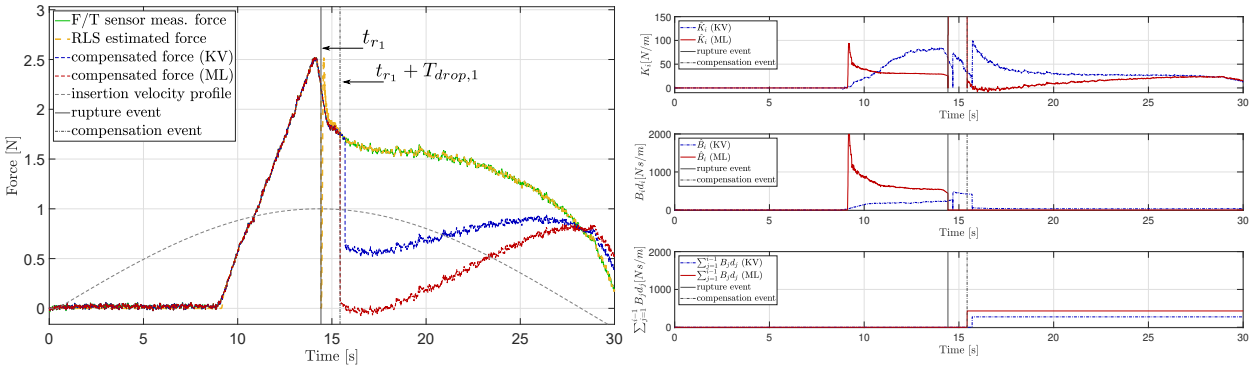

(a) (b)

Fig. 9: Experimental results of the friction compensation algorithm on the 70% solution gel phantom, with unknown layer depth. The needle insertion occurs with a sinusoidal velocity. (a) Measured (green), predicted (yellow) and compensated forces using the KV (blue line) and the ML (red line) models. With vertical black lines are highlighted the rupture detection time t_r (continuous line) and the compensation time $t_r + T_{drop}$ (dashed line). The normalized profile of the sinusoidal velocity is also shown (dashed gray), to highlight its variation along the insertion. (b) Estimation of the elastic (upper panel), local friction (middle panel) and cumulative friction (bottom panel) parameters for the presented experiment.

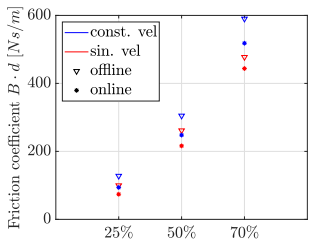

Fig. 10: Comparison of the estimated friction coefficients of the three considered single-layer isinglass phantoms, for constant (blue) and sinusoidal (red) insertion velocity. Triangles denote friction values retrieved from offline analysis, while stars represent parameters estimated through the online identification methodology with covariance re-weighting procedure.

Isinglass phantom	Offline Avg. ± variance (%−error)	Online Avg. ± variance (%−error)
25%	113 ± 14 ($\sim 12\%$)	84 ± 10 ($\sim 12\%$)
50%	283 ± 21 ($\sim 7\%$)	232 ± 16 ($\sim 6.8\%$)
70%	534 ± 56 ($\sim 10\%$)	481 ± 37 ($\sim 7.73\%$)

TABLE I: Average value and variance of the estimated friction for insertions in single-layer isinglass phantoms, evaluated over the two constant and sinusoidal velocity profiles. Units are [Ns/m].

bottom panel reports the cumulative estimated friction term, here equivalent to the friction of the single considered layer.

A second experiment on the same 70% solution gelatin phantom, with sinusoidal insertion velocity, is shown in Fig. 9, where we also show the normalized profile of the insertion velocity to highlight the motion variation with respect to the reported measured force. For the considered motion, we used an amplitude $A = 7$ cm and a frequency equal to $f_{Hz} = 0.016$ Hz. Although none of the two models captures the linearity of the friction component, the ML model succeeds in returning a value of the friction closer to the real one. For this experiment, we observe that the behavior of the compensated force (after the detected rupture at $t_{r_1} \simeq 20$ s) reflects the presence of unmodeled dynamics, already mentioned in Sect. II, that affects the fitting of the selected models with respect to the experimental measured force data, in case of non-constant insertion velocity. In fact, the raising curve observed in Fig. 9a is comparable to the fitting deviation evaluated, for the same class of target phantom, in the bottom panel of Fig.2c. Analogous results are obtained for gelatin phantoms with 25% and 50% solution, reported in the accompanying Supplementary material. The quality of the online estimation results obtained with the ML model are also confirmed in Tab. I and Fig. 10, where we reported a comparison of the estimated friction in the considered single-layer isinglass phantoms, between offline and online estimation procedures. For each phantom, the Table reports

This article has been accepted for publication in a future issue of this journal, but has not been fully edited. Content may change prior to final publication. Citation information: DOI 10.1109/TMRB.2021.3118304, IEEE Transactions on Medical Robotics and Bionics

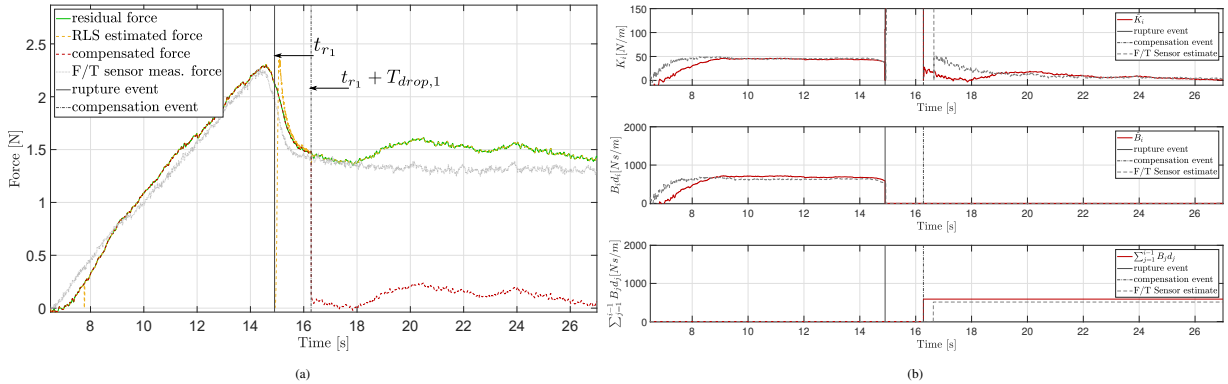

(a) (b)

Fig. 11: Experimental results of the friction compensation algorithm on the 70% solution gel phantom, with unknown layer depth. The needle insertion occurs with a constant velocity. In this experiment, the real F/T sensor is replaced with the virtual sensor based on the momentum-based residual. (a) Estimated (green), predicted (yellow) and compensated forces using the ML (red line) model. F/T measured force is reported in gray for comparison. The vertical black lines highlight the rupture detection time t_r (continuous line) and the compensation time $t_r + T_{drop}$ (dashed line). (b) Estimation of the elastic (upper panel), local friction (middle panel) and cumulative friction (bottom panel) parameters for the presented experiment.

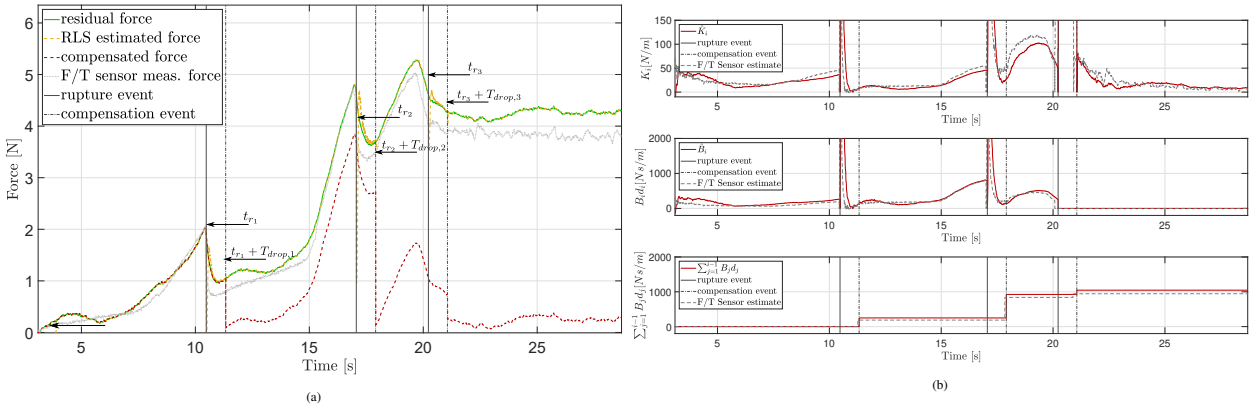

(a) (b)

Fig. 12: Experimental results of the friction compensation algorithm with unknown layer depth of a multi-layer gel target, composed by a 25%, 50% and 70% solution gel layers. A latex glove is placed around the intermediate layer to include additional elastic interaction. The needle is inserted with a constant velocity. In this experiment, the real F/T sensor is replaced with the virtual sensor based on the momentum-based residual: (a) Estimated (green), predicted (yellow) and compensated forces using the ML (red line) model. F/T measured force is reported in gray for comparison. With vertical black lines are highlighted the rupture detection time t_r (continuous line) and the compensation time $t_r + T_{drop}$ (dashed line). (b) Estimation of the elastic (upper panel), local friction (middle panel) and cumulative friction (bottom panel) parameters for the presented experiment.

the average friction value, with variance and corresponding %-wise error, obtained from two insertions with constant and sinusoidal velocity: the obtained results are comparable to the estimations retrieved from the offline analysis, proving the validity of the online identification methodology with covariance re-weighting. In Fig. 10, we also observe that the online friction values underestimate the corresponding values reconstructed from offline analysis. This is explained with possible inaccuracies in the tissue rupture detection: if the detection is delayed with respect to the actual rupture event, the friction $\hat{B}_i(t_{r_i})$ evaluated at the corresponding instant may be slightly below the maximum value assumed at the peak.

The presented results show how the ML model outperforms the KV model in identifying physically plausible friction coefficients of the traversed layers, starting from acquired force measurements of a real F/T sensor. From now on, we will show friction identification and compensation results for the only ML model, starting from the model-based interaction force estimation that acts as a *virtual* F/T sensor.

Figure 11 reports the results for the insertion experiment with constant velocity on the 70% gelatin phantom: with respect to the results shown with the real F/T sensor, our approach performs satisfactorily, as can be appreciated also by observing the estimated values of the coefficients in Fig. 11b, where we report in dashed gray, for comparison, the analogous coefficients estimated in Fig. 8b with the F/T sensor.

A final experiment for this class has been carried out on the three-layered phantom already described in Fig. 3a, with a constant insertion velocity $v = 3$ mm/s. Results are depicted in Fig. 12, showing that three layer ruptures are correctly detected: the first two ruptures (at time $t_{r_1} \simeq 10.5$ s and $t_{r_2} \simeq 16.5$ s) are relative to the rupture of the thin latex layer of the envelope enclosing the middle gelatin layer, while the last detected rupture ($t_{r_3} \simeq 20.5$ s) corresponds to the exit of the needle tip at the opposite point of the entry of the phantom.

While replicating more realistic conditions, the presence of the glove introduces, for each layer i, an artificial nonlinearity in the corresponding force signal, altering the estimation of the thickness $\hat{d}_i$ and resulting in possible misleading estimations of the friction component. This is also reflected in a time-varying behavior of the estimated coefficients within the same layer (see Fig. 12b). However, the estimated values of the coefficients are still suitable enough to guarantee at least a physical feasibility, as confirmed by the resulting *enhanced* force signal that is close to zero after the exit of the needle tip from the phantom.

This article has been accepted for publication in a future issue of this journal, but has not been fully edited. Content may change prior to final publication. Citation information: DOI 10.1109/TMRB.2021.3118304, IEEE Transactions on Medical Robotics and Bionics

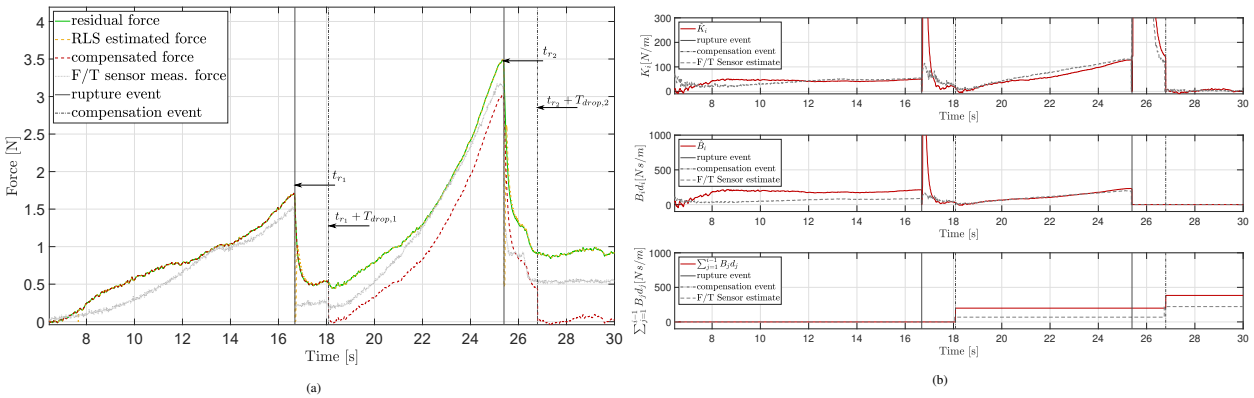

(a) (b)

Fig. 13: Experimental results of the friction compensation algorithm on a bovine liver target of unknown layer depths, moving with constant needle velocity. In this experiment, the real F/T sensor is replaced with the virtual sensor based on the momentum-based residual: (a) estimated (green), predicted (yellow) and compensated forces using the ML (red line) model. F/T measured force is reported in gray for comparison. With vertical black lines are highlighted the rupture detection time t_r (continuous line) and the compensation time $t_r + T_{drop}$ (dashed line). (b) Estimation of the elastic (upper panel), local friction (middle panel) and cumulative friction (bottom panel) parameters for the presented experiment.

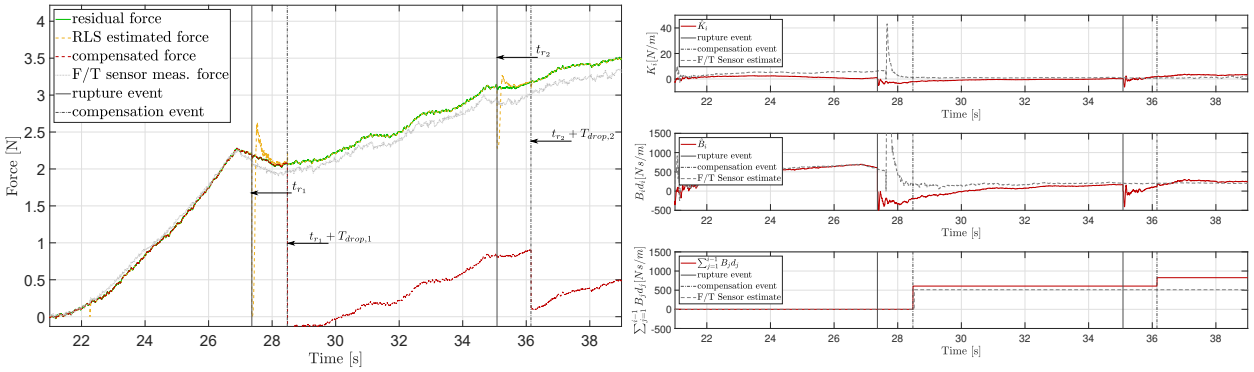

(a) (b)

Fig. 14: Experimental results of the friction compensation algorithm on the abdominal phantom target, with the needle moving with constant velocity. In this experiment, the real F/T sensor is replaced with the virtual sensor based on the momentum-based residual: (a) estimated (green), predicted (yellow) and compensated forces using the ML (red line) model. F/T measured force is reported in gray for comparison. With vertical black lines are highlighted the rupture detection time t_r (continuous line) and the compensation time $t_r + T_{drop}$ (dashed line). (b) Estimation of the elastic (upper panel), local friction (middle panel) and cumulative friction (bottom panel) parameters for the presented experiment.

B. Experiments on real organic tissues

As a second class of insertion targets, we consider a portion of a bovine liver. In this case, a ground truth about the internal geometry is not available, but it is possible to validate a posteriori the identified ruptures by a simple visual inspection of the retrieved/estimated F/T signal.

In Fig. 13, we show the estimation and compensation results for an insertion with constant velocity $v = 2.3$ mm/s, with two layer transitions correctly detected by our algorithm (at $t_{r_1} \simeq 16.5$ s and $t_{r_2} \simeq 25.5$ s).

The presented experiment shows the behavior already described in Sect. III-B: since the liver has an external membrane to be perforated before penetrating the inner tissues, the space between the external contact and the first detected rupture (occurring at $t_{r_1} \simeq 16.5$ s) is identified as a first layer L_1, despite the needle is still outside the liver in that interval. However, the measured force after the rupture is not null, although very low (~ 0.25 N) due to the damping component resulting from the puncturing phase of the layer below.

We also highlight that, despite the model-based force estimation (green line) has a slightly larger value than the F/T sensor measurement (gray line), the identification algorithm will return a friction contribution that allows the enhanced force signal (red line in Fig. 13a) to almost vanish (as expected) when the needle tip entirely traverses the liver. This shows that the identified parameters are consistent in terms of cumulative friction and also account for the model inaccuracies present in the model-based estimation force.

C. Experiments on a medical abdominal phantom

As last category of insertion target, we conducted an experiment on an abdominal phantom, integrating the corresponding 3D model in the simulation scene, as detailed in Sect. V-C, so as to provide a visual reference to observe the progress of the insertion (see Fig. 7). We considered here an insertion with sinusoidal velocity, with $A = 11.5$ cm and $f_{Hz} = 0.02$ Hz. In the planned insertion trajectory, the needle is expected to traverse through simulated fat, muscle and liver layers. Fig. 14 reports the interaction force estimated by the virtual F/T sensor (green line): the first transition in the first fat layer is not detected due to the smooth force segment that does not highlight abrupt changes at the phantom entrance. However, since it is the only external transition, it can be observed through a visual inspection of the insertion in the surgical scenario. Instead, muscle and liver layer transitions are correctly detected at $t_{r_2} \simeq 27.5$ s and $t_{r_3} \simeq 35$ s, with estimated friction components that, after compensation,

generate a feasible *enhanced* force signal.

As a final comment to the presented results, we briefly discuss the presence of negative values that can be observed in the plots of the coefficient estimates for all the described experiments. The estimates, in fact, may assume negative value when the force signal input in the RLS algorithm is negative, both when relying on the F/T sensor and on the momentum-based measurements. In the former case, possible estimation inaccuracies of the cumulative friction term of the previous layers may result in a slight over-compensation after the rupture. Similarly, in the latter case, the cause of the negative values is due to estimation errors resulting from the momentum-based force reconstruction. In both cases, this only occurs during a short transient phase.

A visualization of these experiments, performed with the support of the developed framework and the CoppeliaSim environment, is shown in the accompanying video of the paper.

VII. Conclusions and Future Work

We have presented a novel methodology to predict online the needle-tissue interaction force, to identify and subtract the friction component, in order to generate a reliable *enhanced* force signal during robot-assisted needle insertion procedures.

We first showed how to exploit the mathematical model of the needle-tissue interaction to identify the friction component, by relying on a real F/T sensor located at the robot end-effector. A refinement process with robust online update of the interaction model parameters is described to handle poorly exciting input signals and observability issues.

Next, we described the use of the momentum-based residual signal to realize a virtual F/T sensor and generate a reliable estimation of the force. We showed that friction identification and subtraction can equivalently adopt virtual and real F/T sensors, by providing comparable *enhanced* force signals.

The approach has been validated against ground-truth results obtained offline in a wide array of experiments on different targets.

We aim at integrating the force enhancing algorithm in a teleoperation scheme to provide the operator with the most appropriate haptic rendering of the features of interest in the needle-tissue interaction force. As further improvement, we will complete the integration of a visual simulator in the presented framework for a full visuo-haptic feedback during needle-insertion procedures, by also including virtual reality experience, analogously to what we have done in [27]. We also aim at extending the current simulator functionalities to account for rendering of soft tissues and deformable objects.

References

[1] O. Gerovich, P. Marayong, and A. Okamura, "The effect of visual and haptic feedback on computer-assisted needle insertion," *Computer Aided Surgery*, vol. 9, no. 6, pp. 243–249, 2004.

[2] D. De Lorenzo, Y. Koseki, E. De Momi, K. Chinzei, and A. M. Okamura, "Coaxial needle insertion assistant with enhanced force feedback," *IEEE Transactions on Biomedical Engineering*, vol. 60, no. 2, pp. 379–389, 2013.

[3] "interventional systems," https://www.interventional-systems.com/micromate/.

[4] "Soteria medical," https://www.soteria-medical.com.

[5] "Perfint healthcare," http://www.perfinthealthcare.com/.

[6] "Xact robotics," https://xactrobotics.com/.

[7] A. M. Okamura, C. Simone, and M. D. O'Leary, "Force modeling for needle insertion into soft tissue," *IEEE Transactions on Biomedical Engineering*, vol. 51, no. 10, pp. 1707–1716, 2004.

[8] N. Abolhassani, R. Patel, and M. Moallem, "Needle insertion into soft tissue: A survey," *Medical Engineering & Physics*, vol. 29, no. 4, pp. 413–431, 2007.

[9] D. van Gerwen, "Needle-tissue interaction by experiment," Ph.D. dissertation, TU Delft, 2013.

[10] M. Khadem, C. Rossa, R. Sloboda, N. Usmani, and M. Tavakoli, "Mechanics of tissue cutting during needle insertion in biological tissue," *IEEE Robotics and Automation Letters*, vol. 1, no. 2, pp. 800–807, 2016.

[11] P. Moreira, N. Zemiti, C. Liu, and P. Poignet, "Viscoelastic model based force control for soft tissue interaction and its application in physiological motion compensation," *Computer Methods and Programs in Biomedicine*, vol. 116, no. 2, pp. 52–67, 2014.

[12] L. Barbè, B. Bayle, M. de Mathelin, and A. Gangi, "In vivo model estimation and haptic characterization of needle insertions," *The International Journal of Robotics Research*, vol. 26, no. 11-12, pp. 1283–1301, 2007.

[13] N. Cacciotti, A. Cifonelli, C. Gaz, V. Paduano, A. V. Russo, and M. Vendittelli, "Enhancing force feedback in teleoperated needle insertion through on-line identification of the needle-tissue interaction parameters," in *2018 7th IEEE International Conference on Biomedical Robotics and Biomechatronics (Biorob)*, 2018, pp. 79–85.

[14] M. Aggravi, D. A. L. Estima, A. Krupa, S. Misra, and C. Pacchierotti, "Haptic teleoperation of flexible needles combining 3d ultrasound guidance and needle tip force feedback," *IEEE Robotics and Automation Letters*, vol. 6, no. 3, pp. 4859–4866, 2021.

[15] S. Haddadin, A. De Luca, and A. Albu-Schäffer, "Robot collisions: A survey on detection, isolation, and identification," *IEEE Transactions on Robotics*, vol. 33, no. 6, pp. 1292–1312, 2017.

[16] R. J. Roesthuis, Y. R. J. van Veen, A. Jahya, and S. Misra, "Mechanics of needle-tissue interaction," in *2011 IEEE/RSJ International Conference on Intelligent Robots and Systems (IROS)*, 2011, pp. 2557–2563.

[17] O. Grigg, V. Farewell, and D. Spiegelhalter, "Use of risk-adjusted CUSUM and RSPRT charts for monitoring in medical contexts," *Statistical Methods in Medical Research*, vol. 12, no. 2, pp. 147–70, 2003.

[18] C. Gaz and A. De Luca, "Payload estimation based on identified coefficients of robot dynamics – with an application to collision detection," in *2017 IEEE/RSJ International Conference on Intelligent Robots and Systems (IROS)*, 2017, pp. 3033–3040.

[19] J. Hollerbach, W. Khalil, and M. Gautier, "Model identification," in *Handbook of Robotics*, B. Siciliano and O. Khatib, Eds. Springer, 2008, pp. 321–344.

[20] C. Gaz, F. Flacco, and A. De Luca, "Identifying the dynamic model used by the KUKA LWR: A reverse engineering approach," in *2014 IEEE International Conference on Robotics and Automation (ICRA)*, 2014, pp. 1386–1392.

[21] C. Gaz, M. Cognetti, A. Oliva, P. Robuffo Giordano, and A. De Luca, "Dynamic identification of the Franka Emika Panda robot with retrieval of feasible parameters using penalty-based optimization," *IEEE Robotics and Automation Letters*, vol. 4, no. 4, pp. 4147–4154, 2019.

[22] Coppelia Robotics, "CoppeliaSim." [Online]. Available: http://www.coppeliarobotics.com

[23] N. Aghakhani, M. Geravand, N. Shahriari, M. Vendittelli, and G. Oriolo, "Task control with remote center of motion constraint for minimally invasive robotic surgery," in *2013 IEEE International Conference on Robotics and Automation (ICRA)*, 2013, pp. 5807–5812.

[24] "3D Slicer." [Online]. Available: https://www.slicer.org/

[25] P. J. Besl and N. D. McKay, "A method for registration of 3-d shapes," *IEEE Transactions on Pattern Analysis and Machine Intelligence*, vol. 14, no. 2, pp. 239–256, 1992.

[26] M. Mahvash and P. E. Dupont, "Mechanics of dynamic needle insertion into a biological material," *IEEE Transactions on Biomedical Engineering*, vol. 57, no. 4, pp. 934–943, 2010.

[27] G. A. Fontanelli, M. Selvaggio, M. Ferro, F. Ficuciello, M. Vendittelli, and B. Siciliano, "Portable dVRK: an augmented V-REP simulator of the da Vinci Research Kit," *Acta Polytechnica Hungarica*, vol. 16, no. 8, pp. 79–98, 2019.